

Available online at [www.sciencedirect.com](http://www.sciencedirect.com)

ScienceDirect

journal homepage: [www.elsevier.com/locate/he](http://www.elsevier.com/locate/he)

# Efficiency assessment of solar redox reforming in comparison to conventional reforming



Philipp Holzemer-Zerhusen<sup>a,c,\*</sup>, Stefan Brendelberger<sup>a</sup>,  
Henrik von Storch<sup>b</sup>, Martin Roeb<sup>a</sup>, Christian Sattler<sup>a,c</sup>, Robert Pitz-Paal<sup>a</sup>

<sup>a</sup> Deutsches Zentrum für Luft- und Raumfahrt, Institute of Solar Research, Linder Höhe, 51147, Köln, Germany

<sup>b</sup> Deutsches Zentrum für Luft- und Raumfahrt, Institute of Solar Research, Karl-Heinz-Beckurts-Str.13, 52428, Jülich, Germany

<sup>c</sup> TU Dresden, Faculty of Mechanical Science and Engineering, Institute of Power Engineering, Professorship of Solar Fuel Production, 01062, Dresden, Germany

## HIGHLIGHTS

- Solar redox reforming and solar conventional reforming are simulated.
- Iron oxide and ceria-based redox cycles are compared.
- Efficiency and product quality are evaluated.
- Impact of solar flux and solid-solid heat recovery is analyzed.

## ARTICLE INFO

### Article history:

Received 10 September 2019

Received in revised form

26 November 2019

Accepted 11 December 2019

Available online 9 January 2020

### Keywords:

Reforming

Redox cycle

Synthesis gas

Ceria

Iron oxide

Solar fuels

## ABSTRACT

Solar redox reforming is a process that uses solar radiation to drive the production of syngas from natural gas. This approach caught attention in recent years, because of substantially lower reduction temperatures compared to other redox cycles. However, a detailed and profound comparison to conventional solar reforming has yet to be performed. We investigate a two-step redox cycle with iron oxide and ceria as candidates for redox materials. Process simulations were performed to study both steam and dry methane reforming. Conventional solar reforming of methane without a redox cycle, i.e. on an established catalyst was used as reference. We found the highest efficiency of a redox cycle to be that of steam methane reforming with iron oxide. Here the solar-to-fuel efficiency is 43.5% at an oxidation temperature of 873 K, a reduction temperature of 1190 K, a pressure of 3 MPa and a solar heat flux of 1000 kW/m<sup>2</sup>. In terms of efficiency, this process appears to be competitive with the reference process. In addition, production of high purity H<sub>2</sub> or CO is a benefit, which redox reforming has over the conventional approach.

© 2019 Hydrogen Energy Publications LLC. Published by Elsevier Ltd. All rights reserved.

\* Corresponding author. Deutsches Zentrum für Luft- und Raumfahrt, Institute of Solar Research, Linder Höhe, 51147, Köln, Germany.  
E-mail address: [Philipp.Holzemer-Zerhusen@dlr.de](mailto:Philipp.Holzemer-Zerhusen@dlr.de) (P. Holzemer-Zerhusen).

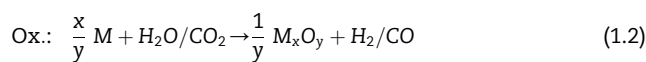
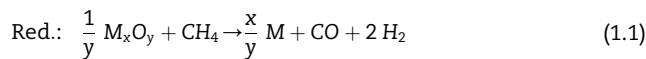
<https://doi.org/10.1016/j.ijhydene.2019.12.065>

0360-3199/© 2019 Hydrogen Energy Publications LLC. Published by Elsevier Ltd. All rights reserved.

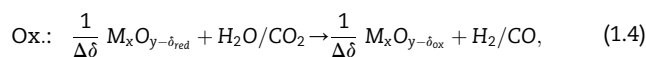
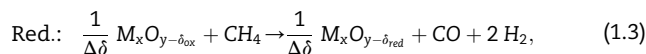
## Introduction

In the field of renewable fuel production, redox cycles for splitting  $H_2O$  or  $CO_2$  are frequently investigated. Commonly these processes include a thermal reduction step, in which a redox material is regenerated after its oxidation in an  $H_2O$  or  $CO_2$ -splitting step [1–9]. A major drawback of these redox cycles is that the requirements for reaching high reduction extents of the redox material are very demanding. These requirements are mainly a very high reduction temperature (ca. 1773 K for a typical ceria cycle [10–12]) and removal of large quantities of released oxygen at low partial pressures. This makes achieving high process efficiencies challenging and also leads to practical difficulties, when it comes to properties of the building materials for example. To reduce the necessary temperature, while maintaining a significant degree of reduction, the oxygen partial pressure in the reduction reactor has to be decreased. In case of thermal reduction this is commonly done, by sweeping with an inert gas or by vacuum pumping [2–4,13–20].

In redox reforming methane from natural gas is introduced as a reductant, which reacts with the released oxygen forming carbon monoxide. In other words, the reductant can be interpreted as an oxygen sink, which yields substantially lower partial pressures of oxygen compared to inert gas sweeping and vacuum pumping [21]. Consequently the necessary reduction temperature decreases significantly [22]. While in a thermal reduction pure oxygen is removed from the reactor, the reduction step with methane produces a syngas with an  $H_2$ :CO-ratio of 2:1. This is shown in Equations (1.1) and (1.3). Equation (1.1) is the reduction of a stoichiometric redox material. The associated oxidation reaction is given in Equation (1.2). Here,  $M$  represents any metal atom.



Alternatively the redox cycle can be conducted with a non-stoichiometric redox material, such as some perovskites [23] or ceria [13]. Those materials undergo a smooth transition between reduced and oxidized state as described in detail in the relevant literature [13,23–26]. The non-stoichiometry  $\delta$  characterizes the oxidation state of such a material according to



where  $\delta_{red}$  and  $\delta_{ox}$  are the non-stoichiometry at reduced and oxidized state, respectively and  $\Delta\delta = \delta_{red} - \delta_{ox}$ . When adding the aforementioned reduction and oxidation steps, the net reaction equals that of well-established conventional reforming processes. These are namely steam methane reforming (SMR) in case of  $H_2O$ -splitting and dry methane reforming (DMR) in case of  $CO_2$ -splitting.

Sheu et al. [27,28] performed simulations on redox reforming. They identified iron/magnetite as a promising redox material. In their investigations they analyze the efficiency of a hybrid power plant integrating both redox SMR and DMR. The overall cycle efficiencies of the combined cycle power plant with upstream solar redox reforming was found to be in the order of 51–54% for SMR and 54–56% for DMR [28] for different solar shares. He et al. [22] investigated redox SMR with an iron oxide-based redox material. The reduction was integrated in a process for the coproduction of  $H_2$  and liquid fuels in a Fischer-Tropsch reactor [29]. The resulting process efficiency was estimated to be 64.2 HHV%. Application of ceria as redox material was studied by Warren et al. [30] both theoretically and experimentally. Herein theoretical solar-to-fuel efficiencies of more than 45% were calculated, while experiments with a packed bed of ceria in a solar cavity receiver yield an efficiency of up to 2.8%. This value was extrapolated for a larger reactor capacity to a value of up to 9.8%. Welte et al. [31] performed experiments on redox reforming in a solar driven particle reactor. They studied the reduction of ceria with methane in co-current and counter-current flow through an  $Al_2O_3$  tube in a 2 kW<sub>th</sub> reactor. The main drawback of a counter-current arrangement was the reaction of ceria and product gas. The peak solar to fuel efficiency, assuming full re-oxidation with  $CO_2$  was 12% at a tube temperature of 1576 K. At tube temperatures above 1573 K carbon formation was suppressed. Direct comparison of the above-mentioned efficiencies is not always possible. They are obtained from different processes and also vary slightly in their definitions. However they show the general potential of redox reforming and motivate further investigation.

Since redox reforming utilizes methane and thereby depends on a fossil carbon source, it does not operate in a closed carbon cycle. It is therefore only justified if a higher solar-to-fuel efficiency or other significant benefits are achieved compared to conventional solar reforming. While the aforementioned studies yield valuable insights into the process, a detailed comparison between redox reforming and conventional reforming is yet to be performed. With the present study we want to provide a fair and founded comparison of the two alternatives. We investigate the application of solar power in both conventional and redox reforming and take into account that hydrogen and syngas are commonly needed at high pressures. Aspen Custom Modeler is used for the flow-sheet simulations.

## Models

### Processes and flowsheets

Simulations for six different systems are performed. These are namely redox-cycles with iron oxide and ceria for both SMR and DMR and conventional SMR and DMR. The latter are established processes, which we use as references. For both redox materials and for the conventional approach reactor models are derived and implemented in Aspen Custom Modeler V10 (ACM) by AspenTech, while for other unit operations the built-in models of the Aspen libraries are used.

These sub-models are connected to form the flowsheets given in Fig. 1 and Fig. 2.

A central target of the present study is to calculate the efficiency of the studied processes under comparable conditions for several points of operation. To do so, the flowsheets are designed such that the product always leaves the process with 3 MPa, independent of the pressure in the reactors. That way the compression work that is necessary to generate a pressurized product is always taken into account, which means the efficiencies of all process alternatives are calculated for comparable products. As can be seen in the flowsheets below, the feed stream is first compressed to the reformer pressure and downstream of the reaction further to 3 MPa. Compressors shown in Figs. 1 and 2 represent a set of up to 4 compressors with intermediate cooling steps to prevent an excessive expansion of the gas, keeping the compression work at moderate values. Herein one compressor has a maximum outlet to inlet pressure ratio of 3. The reforming pressure has an important impact on the efficiency, which is explained later in the results section. In our redox cycle models we always set the same pressure in reduction and oxidation reactors.

Another key quantity is the temperature in the reactors. In case of redox reforming, the temperature in the reduction reactor is chosen such that together with a variable reformer pressure a certain methane conversion is achieved. The temperature in the oxidation reactor is the second variable and together with the reforming pressure it defines the point of operation.

The flowsheets and reactor models for redox reforming and reference processes are similar in their degree of complexity. Along with the aforementioned constant product pressure, this allows direct comparison of calculated efficiencies. As a metric for our discussion, the solar-to-fuel efficiency  $\eta_{STF}$ , based on the higher heating value (HHV) is used. It is defined as

$$\eta_{STF} = \frac{\Delta HHV}{\frac{P_{comp}}{\eta_{field} \cdot \eta_{PB}} + \frac{\dot{Q}_{solar}}{\eta_{field}}}, \quad (2.1)$$

where  $\Delta HHV$  is the change in the HHV during the reaction,  $P_{comp}$  is the sum of all compressors' power,  $\dot{Q}_{solar}$  is the solar heat flux as it reaches the reactor,  $\eta_{field}$  is the efficiency of the heliostat field and  $\eta_{PB}$  is the power block efficiency of a solar

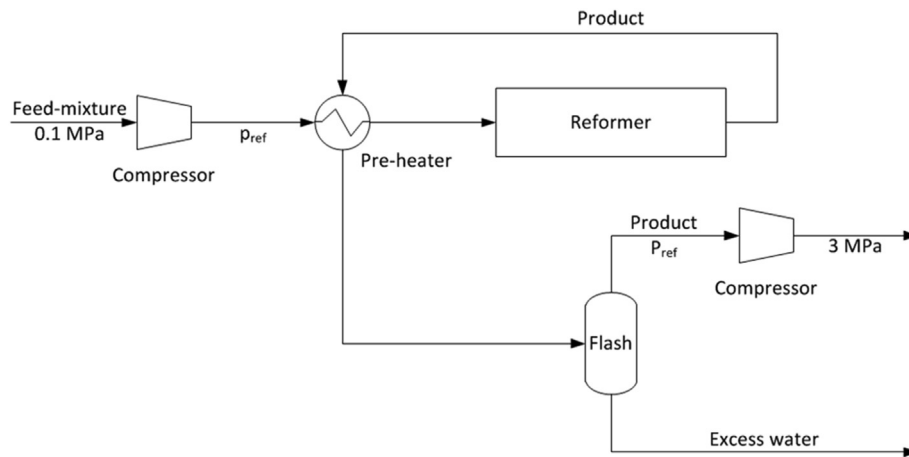


Fig. 1 – Simplified flowsheet of the reference models.

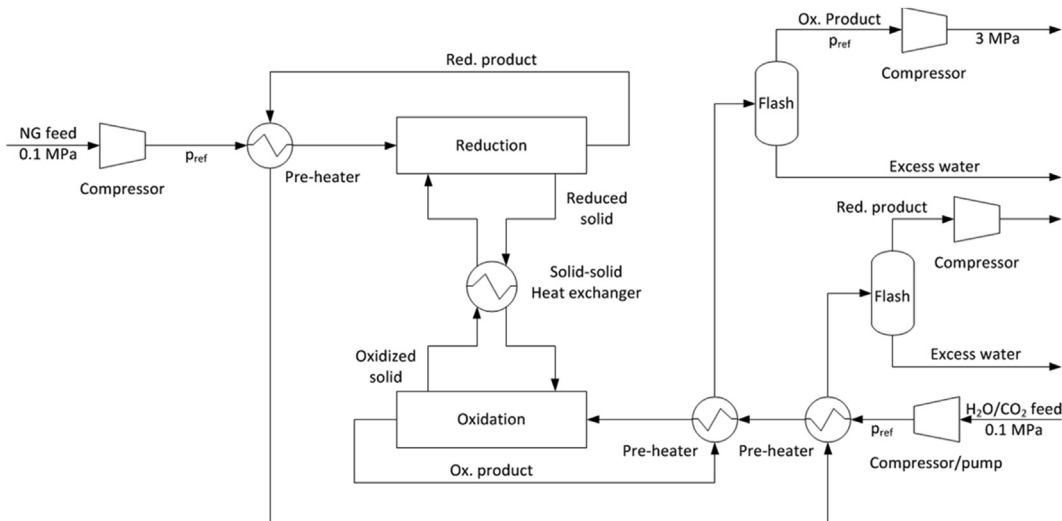


Fig. 2 – Simplified flowsheet of redox cycles.

power plant. It is assumed that the compressor power is supplied by a solar power plant with the same field efficiency. For the power block,  $\eta_{PB} = 0.4$  seems to be a realistic value [32,33].  $\Delta HHV$  is calculated according to

$$\Delta HHV = \Delta \dot{n}_{H_2} \cdot HHV_{H_2} + \Delta \dot{n}_{CO} \cdot HHV_{CO} + \Delta \dot{n}_{CH_4} \cdot HHV_{CH_4} \quad (2.2)$$

with

$$\Delta \dot{n}_i = \dot{n}_{i,product} - \dot{n}_{i,feed} \quad (2.3)$$

For redox reforming both reactors, i.e. reduction and oxidation chamber might need a solar input flux and both create a change in HHV, so that  $\dot{Q}_{solar} = \dot{Q}_{solar,red} + \dot{Q}_{solar,ox}$  and  $\Delta HHV = \Delta HHV_{red} + \Delta HHV_{ox}$ .

### Reactors

Reactors are modelled as directly irradiated receiver reactors with an absorptivity and emissivity of 1, hence assuming that the receiver is a black body. The heat flux density that is received from the collector is given as a fixed value of either 1500 or 1000 kW/m<sup>2</sup>. Unless stated otherwise, 1500 kW/m<sup>2</sup> are applied. The reduction reactor is always powered by solar radiation through an aperture, whereas for the oxidation the need to be heated and hence the need of an aperture depends on the operating conditions. If an aperture is necessary, it is sized according to the heat demand. Consequently, it is scaled in relation to the aperture of the reduction reactor. The reactor models are generic, i.e. the design of the reactor is not considered. For all processes, the reaction is modelled as an equilibrium reaction at given temperature and pressure. We use a lumped model for the reactor not taking spatial resolution into account.

### Redox materials

The reduced and oxidized states of Iron oxide considered in this study are Fe and Fe<sub>3</sub>O<sub>4</sub>, respectively, as in several other studies [27,28,34,35]. A higher degree of oxidation than Fe<sub>3</sub>O<sub>4</sub>, such as Fe<sub>2</sub>O<sub>3</sub> doesn't seem to be reached in the oxidation step [36]. The reduction to metallic Fe was observed in experiments [35]. Furthermore, equilibrium-calculations with the software FactSage 7.0 [37] imply that the main product of the reduction with methane is metallic Fe. Formation of FeO is therefore not considered.

Unlike iron oxide, ceria shows a non-stoichiometric behavior. This can be modelled, using continuous oxidation states represented by the quantity  $\delta \in [0, 0.35]$ . Since no such material-behavior is preinstalled in the simulation tools, a mixture of CeO<sub>2</sub> and Ce<sub>2</sub>O<sub>3</sub> is used to define the material stream of ceria in ACM. However, this is only relevant for the energy balance of the reactor, while the thermodynamics of the reaction are calculated using  $\delta$  as will be described later. Using a mixture of CeO<sub>2</sub> ( $\delta = 0$ ) and Ce<sub>2</sub>O<sub>3</sub> ( $\delta = 0.5$ ) results in a linear interpolation of the enthalpy between these two states of oxidation. To justify this choice we validate the approach with data from the software FactSage 7.0 [37], which contains data for two more states of oxidation ( $\delta \approx 0.17$  and  $\delta \approx 0.29$ ). Fig. 3 depicts the discrepancy between linear interpolation and discrete values from FactSage. The largest deviation ap-

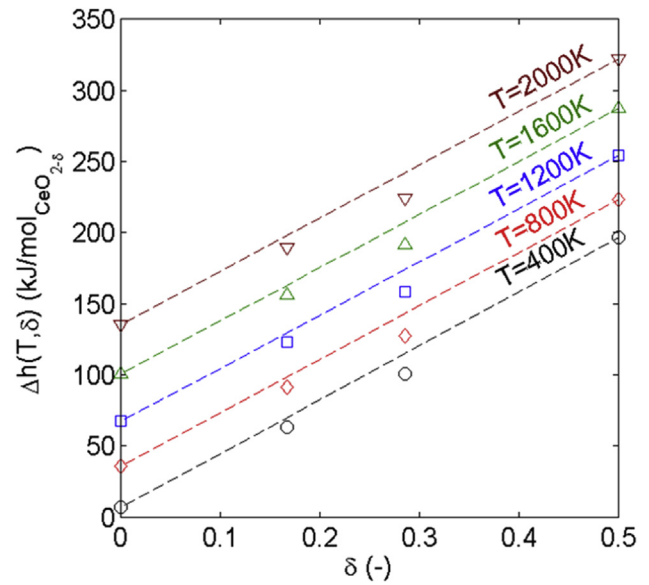


**Fig. 3 – Enthalpy of ceria as function of temperature and  $\delta$ .  $\Delta h(T, \delta) = h(T, \delta) - h(300 \text{ K}, \delta = 0)$ . Dashed lines show the linear interpolation between CeO<sub>2</sub> and Ce<sub>2</sub>O<sub>3</sub>. Marked points show data for different oxidation states obtained from FactSage 7.0.**

pears to be at  $\delta \approx 0.29$ . For a typical calculation with this value, using an oxidation temperature of 800 K, a reduction temperature of 1200 K,  $\delta_{ox} = 0$  and  $\delta_{red} = 0.29$  we find a relative difference of 11% between interpolation and discrete value, while for lower values of  $\delta$  the error seems to be smaller, as can be seen in Fig. 3.

### Reactions

Reactions (1.1)–(1.4) can be described as superposition of the reduction of the redox material given by either



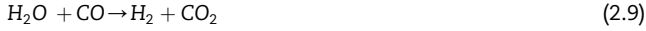
or



and the following gas-phase reactions:



Reactions (2.4) and (2.5) are combined with the partial oxidation of methane (2.6) to describe the reduction or with the splitting reactions of water (2.7) or carbon dioxide (2.8) to describe the respective oxidation. The water gas shift (WGS) reaction does not necessarily have to be considered, since it can be obtained by combining reactions (2.7) and (2.8).



However, the right choice of linear independent reactions has an impact on the convergence of the equation system and thus we chose reactions (2.7) and (2.9) to describe SMR and (2.7) and (2.8) for DMR. Reaction equilibria are determined using the standard Gibbs energy of reaction

$$\Delta_R G^0 = -RT \ln \left( \prod_i \frac{p_i^{v_i}}{p_0} \right), \quad (2.10)$$

where  $p_i$  is the partial pressure of a gas component,  $v_i$  is the stoichiometric factor and  $p_0 = 1 \text{ bar}$  is the standard pressure. The standard Gibbs energy of reaction  $\Delta_R G^0$  is determined with substance data available in ACM. Equation (2.10) can be applied for all the aforementioned reactions. However, the non-stoichiometric behavior of ceria makes it unpractical to use Equation (2.10) on Reaction (2.5), which is why we use the correlation presented by Bulfin et al. [2] to obtain the equilibrium  $\delta$  as a function of the temperature and oxygen pressure. The conversion of  $\text{CH}_4$ ,  $\text{H}_2\text{O}$  and  $\text{CO}_2$ , respectively is defined as

$$X_i = \frac{\dot{n}_{i,\text{feed}} - \dot{n}_{i,\text{product}}}{\dot{n}_{i,\text{feed}}}. \quad (2.11)$$

### Balance equations

The reactor models are completed by introducing mass balances for components and the total amount and an energy balance for the receiver reactor. Component mass balances are given by

$$\dot{n}_i^{\text{out}} - \dot{n}_i^{\text{in}} = \sum_j \nu_{ij} \cdot \xi_j, \quad (2.12)$$

where  $i$  are the components,  $j$  are the reactions and  $\xi_j$  are the reaction extents and  $\nu_{ij}$  are the stoichiometric factors. The overall mass balance of a phase (solid or gas) is

$$0 = \dot{M}_{\text{feed}} \cdot \dot{n}_{\text{feed}} - \dot{M}_{\text{product}} \cdot \dot{n}_{\text{product}} \pm \nu_{\text{O}_2} \cdot \dot{M}_{\text{O}_2} \cdot \xi_{\text{solid}}, \quad (2.13)$$

where the molar mass  $M_i$  is calculated with built-in ACM-functions.  $\xi_{\text{solid}}$  describes the reduction or oxidation, according to Reactions (2.4) and (2.5).

The energy balance reads

$$0 = \dot{Q}_{\text{rec}} + \dot{Q}_{\text{gas}} + \dot{Q}_{\text{solid}} + \dot{Q}_{\text{rr}}. \quad (2.14)$$

herein the heat that reaches the receiver  $\dot{Q}_{\text{rec}}$ , the enthalpy flows of gas and solids, including conversion of matter  $\dot{Q}_{\text{gas}}$  and  $\dot{Q}_{\text{solid}}$  and losses due to reradiation through the aperture  $\dot{Q}_{\text{rr}}$  are considered. Those quantities can be calculated using

$$\dot{Q}_{\text{rec}} = A_{\text{ap}} \cdot \dot{q}_{\text{solar}}, \quad (2.15)$$

$$\dot{Q}_{\text{gas}} = \dot{n}_{\text{gas},\text{in}} \cdot h_{\text{gas},\text{in}} - \dot{n}_{\text{gas},\text{out}} \cdot h_{\text{gas},\text{out}}, \quad (2.16)$$

$$\dot{Q}_{\text{solid}} = \dot{n}_{\text{solid},\text{in}} \cdot h_{\text{solid},\text{in}} - \dot{n}_{\text{solid},\text{out}} \cdot h_{\text{solid},\text{out}}, \quad (2.17)$$

$$\dot{Q}_{\text{rr}} = A_{\text{ap}} \cdot \sigma \cdot T^4, \quad (2.18)$$

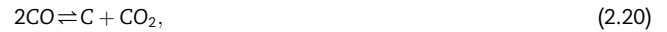
where  $A_{\text{ap}}$  is the aperture area,  $\dot{q}_{\text{solar}}$  is the heat flux from the field and  $h$  is the molar enthalpy of a mole flow. Other losses than reradiation are neglected, as the purpose of this study is

rather to identify the processes' potential than to provide an exact calculation of the heat demand. Also the generic character of the models doesn't allow for proper determination of e.g. convective heat losses.

### Coking potential

Coking is the formation of a dense carbon layer on top of a catalyst or the redox material, which blocks the reactive surface [38]. This deactivates the material and makes it not reusable for further cycles [39]. We therefore want to avoid coking under all circumstances and check the possibility of its occurrence for each point of operation.

There are three mechanisms that lead to carbon formation: pyrolysis of methane, disproportionation of  $\text{CO}_2$  (Boudouard reaction) and the reduction of CO, according to



To estimate the coking potential in the reactors, we follow the principle of equilibrated gases that was applied for conventional reforming by Rostrup-Nielsen et al. [40]. Coking is expected, if the formation of carbon according to Reactions (2.19)–(2.21) is possible, after the equilibrium of the reforming reaction is established. To quantify the coking potential we introduce the coking number  $\Psi$ . It defines how Reactions (2.19)–(2.21) deviate from their equilibrium with

$$\Psi_{\text{MC}} \cdot K_{\text{MC}} \cdot p_{\text{CH}_4} = p_{\text{H}_2}^2, \quad (2.22)$$

$$\Psi_{\text{BOU}} \cdot K_{\text{BOU}} \cdot p_{\text{CO}}^2 = p_{\text{CO}_2}, \quad (2.23)$$

$$\Psi_{\text{COR}} \cdot K_{\text{COR}} \cdot p_{\text{CO}} \cdot p_{\text{H}_2} = p_{\text{H}_2\text{O}}, \quad (2.24)$$

where  $K_{\text{COR}}$ ,  $K_{\text{MC}}$  and  $K_{\text{BOU}}$  are the equilibrium constants of Reactions (2.19)–(2.21). Thus  $\Psi = 1$  indicates equilibrium of the coking reaction, while for  $\Psi < 1$ , the equilibrium is on the product side and hence carbon is formed. If on the other hand  $\Psi > 1$ , reactions (2.19)–(2.21) are reversed, and no coking takes place. Consequently,  $\Psi \geq 1$  indicates that no carbon is formed.

### Field layout

HFLCAL was used to determine the field efficiency at 1000 and 1500 kW/m. The software is described in detail by Schwarzbözl et al. [41]. We choose a site at latitude  $28^\circ \text{N}$ , which corresponds to a North African or Middle Eastern country. The field is designed for 50 MW intercept input using Hottel Method [42]. Powell's method [43] was applied for the field layout optimization.

### Model constraints

Preliminary simulation runs were executed to gain a deeper understanding of the system's behavior. With that we identified constraints, which define a suitable framework for the actual simulations.



It seems intuitive to reduce and oxidize the redox material in the respective reactors to the largest possible extent, hence fully utilizing its oxygen capacity. That way the necessary amount of redox material and the sensible heat that it needs to reach the reduction temperature are reduced. In case of iron oxide we therefore decided to set the molar fraction of Fe at the reduction outlet and that of  $\text{Fe}_3\text{O}_4$  at the oxidation outlet to 0.999. In the reduction of ceria however, coking is evident at large degrees of reduction ( $\delta_{\text{red}} \rightarrow 0.35$ ). Therefore the constraint to specify a certain degree of reduction is replaced by setting  $\Psi_{\text{min}}^{\text{red}} = 1$ . Here the subscript min refers to the minimum value of the three coking mechanisms.

In the oxidation of ceria the coking number typically varies widely with changing temperatures. Setting  $\Psi_{\text{min}}^{\text{ox}} = 1$ , also excludes beneficial points of operation with very high coking numbers, i.e. low coking potential. Thus it is not an expedient constraint. Fixing the value for  $\delta_{\text{ox}}$  is problematic, too: the non-linear oxidation behavior of ceria results in a drastic increase of the  $\text{H}_2\text{O}$  or  $\text{CO}_2$  demand in the reactor, while the related conversion decreases accordingly, with increasing temperature. Alternatively we decided to control the gas-phase composition, by setting a fixed  $\text{H}_2\text{O}$  or  $\text{CO}_2$ -conversion. This value is varied as described later on.

In all processes the conversion of  $\text{CH}_4$  was set to 94.2%. This value was determined with the conventional process model and results in a  $\text{CH}_4$  content in the product below approximately 1.5%, which is a common value in conventional reforming [44].

## Results and discussion

To reach the aforementioned methane conversion of 94.2% at increasing pressures, higher temperatures in the reformer (in case of conventional reforming) or in the reduction chamber (in case of redox reforming) are necessary. Therefore in the following discussion higher reformer or reduction temperatures correspond to higher pressures in the process. The dependence of the temperature on the pressure is different for the different processes as shown in Fig. 4. This effect is relatively small for redox reforming with iron oxide. The process needs potentially lower temperatures than the conventional approach. In case of ceria on the other hand the effect is stronger. Higher temperatures are needed than in conventional reforming. A pressure of approximately 2 MPa can't be exceeded if the high methane conversion shall be maintained. At this point the temperature is so high that the receiver has reached its thermal equilibrium, i.e. reradiation losses consume 100% of the solar input.

The solar-to-fuel efficiency of the conventional process as a function of the temperature is depicted in Fig. 5. The graph reveals an ideal temperature for both processes, which can be explained as follows. At high temperatures reradiation losses rise proportionally to  $T_{\text{ref}}^4$ , while at lower temperatures the energy penalty associated with compression rises. As explained above, lower temperatures are associated with lower pressures. Those result in a shift of the compression work from the compressors upstream of the reformer to those downstream of the reformer. Since the number of moles increases in the reformer this leads to a net increase of the

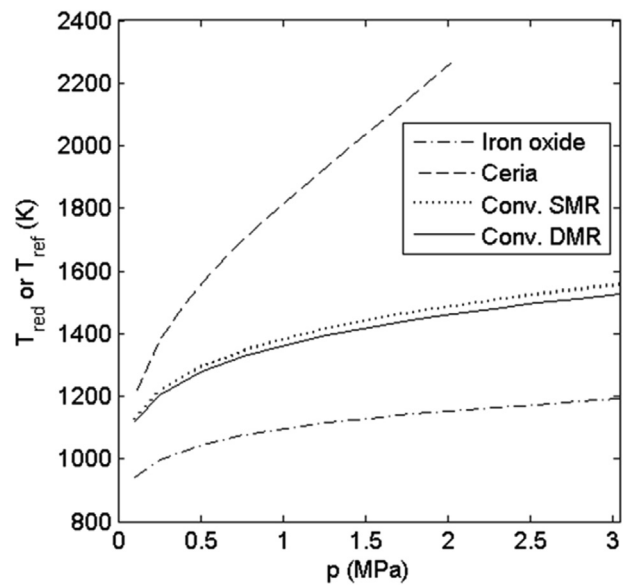


**Fig. 4 – Temperature as function of the reduction pressure. In case of redox reforming the reduction temperature is shown. For conventional SMR and DMR the reformer temperature is shown.**

compression work. A maximum efficiency of 42.5% at 1488 K and 2 MPa for SMR and a maximum efficiency of 38.1% at 1420 K and 1.5 MPa for DMR are found.

In redox reforming the solar-to-fuel efficiency depends on both the temperature in the reduction chamber  $T_{\text{red}}$  and in the oxidation chamber  $T_{\text{ox}}$ . In case of redox SMR with iron oxide this relation is given in Fig. 6. We find the highest efficiencies at high  $T_{\text{red}}$ . A distinct maximum as shown for conventional reforming was however not found. This is because we stop the simulation at a pressure of 3 MPa. Even higher temperatures than those shown in the diagram would either result in higher

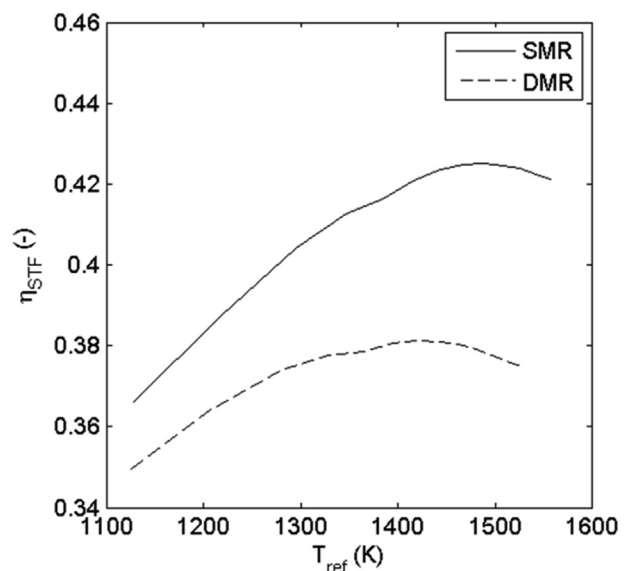


**Fig. 5 – Solar-to-fuel efficiency of conventional SMR and DMR as a function of the reformer temperature.**

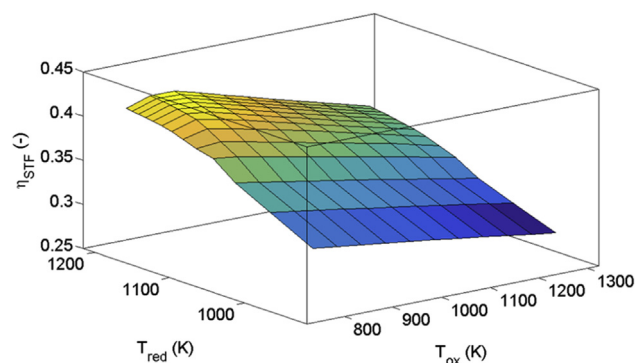


**Fig. 6** – Solar-to-fuel efficiency of redox SMR with iron oxide as a function of reduction and oxidation temperature.

pressures or higher methane conversions. Both mean higher product quality and hence higher  $T_{red}$  are worthwhile. However, to maintain comparability we stay within the bounds of the given constraints and don't investigate these points of operation.

Furthermore, we find that even though the oxidation reaction is exothermal, the oxidation chamber needs to be irradiated. This heat demand is mainly associated with evaporation and superheating of water. The preheaters shown in the flowchart above are not sufficient for that task unless low oxidation temperatures and high reduction temperatures are applied to the system. This result is in agreement with Sheu et al. [27]. They find heating of the oxidation chamber to be necessary at oxidation temperatures well above 800 K, while in our case heating is needed if the oxidation temperature exceeds a value of 773–873 K, depending on the reduction temperature. Consequently, at most points of operation, the oxidation chamber is equipped with an aperture, through which reradiation losses occur. Together with a decreasing  $H_2O$ -conversion at higher oxidation temperatures, these losses cause the decrease in efficiency.

At high reduction temperatures, Fig. 6 reveals an optimum oxidation temperature, below which the efficiency decreases. We account this effect to the sensible heating of the redox material that is fed from the relatively cold oxidation chamber into the hotter reduction chamber. All in all the maximum efficiency of redox SMR with iron oxide found under the specified conditions is 41.9% at a reduction temperature of 1190 K, an oxidation temperature of 873 K and a pressure of 3 MPa.

The most obvious difference between redox DMR with iron oxide and the other redox cycles that we investigate is that the oxidation reaction is endothermal. Consequently the oxidation reactor is always allothermal and has to be irradiated. This leads to an optimum oxidation temperature, which results from a trade-off between a low conversion at low oxidation temperatures and high reradiation losses at high oxidation temperatures. This is shown in Fig. 7. Similar to the efficiency of the conventional process we also find an optimum reduction temperature. The resulting peak solar-to-fuel efficiency is 29.8% at a reduction temperature of 1130 K, an oxidation temperature of 1273 K and a pressure of 1.5 MPa.

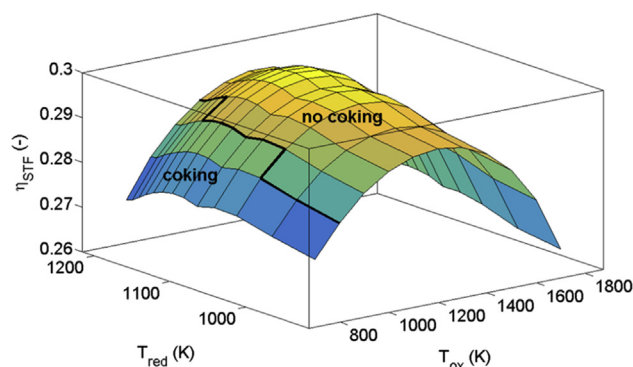


**Fig. 7** – Solar-to-fuel efficiency of redox DMR with iron oxide as a function of reduction and oxidation temperature. The black line marks under which conditions coking is evident in the oxidation reactor.

Fig. 7 reveals some small discrete changes of the slope with respect to  $T_{red}$ . This is caused by the compressor array. Since a single compressor shall not exceed a compression ratio of 3 to avoid excessive compression work, an additional compressor is activated at 0.3, 0.9 and 2.7 MPa. As a result the slope of the efficiency changes at these points, which is evident in all processes, but most apparent in Fig. 7.

As mentioned above, coking in the oxidation with  $CO_2$  is not prevented by model constraints. Therefore the coking number has to be checked for each point of operation. In Fig. 7 points on the black line and below suffer from coking. We find that the formation of carbon occurs at low oxidation temperatures and high reduction temperatures. Limiting factor is the Boudouard reaction (2.20). In this mechanism the formation of carbon is exothermal and accompanied by a decrease of moles in the gas phase. Hence, according to Le Chatelier's principle [45], low oxidation temperatures and high pressures, i.e. high reduction temperatures favor the formation of carbon. Nevertheless especially the most efficient points of operation don't show coking.

Redox reforming was also modelled with ceria as oxygen carrier. Results are given in Fig. 8 and Fig. 9. Note that for the sake of clarity the temperature-scales in Figs. 8 and 9 are inverted compared to Figs. 6 and 7. In accordance with the discussion above, reduction of ceria needs higher

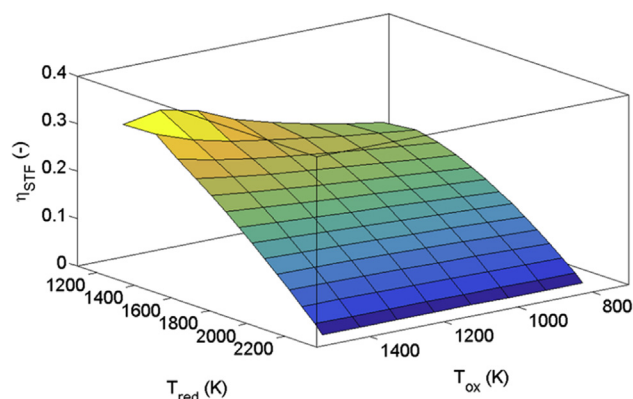


**Fig. 8** – Solar-to-fuel efficiency of redox SMR with ceria as a function of reduction and oxidation temperature.

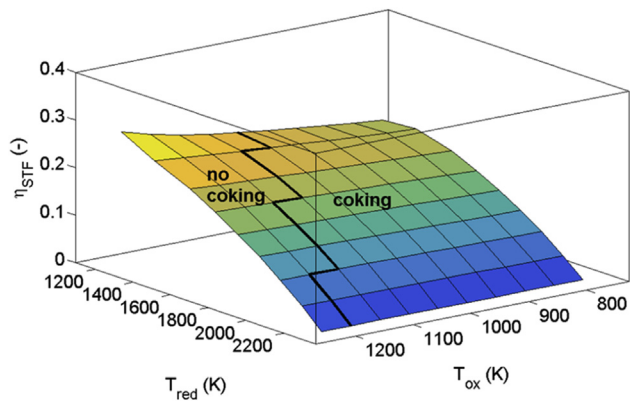


**Fig. 9** – Solar-to-fuel efficiency of redox DMR with ceria as a function of reduction and oxidation temperature. The black line marks under which conditions coking is evident in the oxidation reactor.

temperatures than reduction of iron oxide. Hence it is operated in a domain, where reradiation dominates other impacts on the solar-to-fuel efficiency. Consequently, the highest efficiencies are found at the lowest reduction temperatures. According to Figs. 8 and 9, even lower temperatures than those investigated could be of interest. These temperatures correspond to pressures below 0.1 MPa and are excluded since vacuum operation is beyond the scope of the present study. In the temperature range shown in Figs. 8 and 9 the oxidation temperature only has a minor impact on efficiency for most points of operation. Only at relatively low reduction temperatures we find a maximum efficiency with respect to the oxidation temperature. Interestingly the process is most efficient at high oxidation temperatures, even though the oxidation is exothermal for both SMR and DMR. Similar to SMR with iron oxide we account this effect to the decreased sensible heat demand for heating the redox material to the reduction temperature. We even reach points at which the oxidation temperature exceeds the reduction temperature. In that case the hot material from the oxidation reactor can be interpreted as an additional heat source fed to the reduction chamber, further increasing the efficiency. However, this effect has its limits, since very high oxidation temperatures in combination with low reduction temperatures require irradiation of the oxidation chamber. Hence, an aperture is necessary, resulting in additional reradiation losses.

A side effect of the high oxidation and low reduction temperatures is a small change in the oxidation state between the two reaction chambers, i.e. high efficiencies are observed when  $\Delta\delta$  is low. For the highest efficiencies shown in Figs. 8 and 9  $\Delta\delta \approx 0.1$ , while on average  $\Delta\delta \approx 0.3$ . If the oxidation temperature is raised to values even higher than those shown in Figs. 8 and 9, the decreasing  $\Delta\delta$  leads to increasing amounts of ceria, needed to maintain the oxygen capacity of the material. This again increases the demand for sensible heat.

Obviously, the process is only feasible if  $\delta_{red} > \delta_{ox}$  and consequently there is a limit on the oxidation temperature, since for  $T_{ox} \gg T_{red}$  at some point  $\delta_{red} = \delta_{ox}$  is reached. Practically the model typically stops converging at oxidation temperatures somewhat lower than this limit. This might result

from a constraint that can't be fulfilled or numerical difficulties arise associated with the drastically increasing amount of ceria.

Therefore, higher oxidation temperatures are not included in Figs. 8 and 9, but they are discussed in the following section, where we take a closer look at high oxidation temperatures, which result in areas with high efficiencies and discuss higher conversions during the oxidation.

Analogous to the oxidation of iron oxide with  $\text{CO}_2$ , in the oxidation of ceria with  $\text{CO}_2$  coking is observed. This is again visualized by a black line included in Fig. 9. Coking is evident for many points of operation, however not for the most efficient ones at high oxidation temperatures. Again, the Boudouard reaction (2.20) causes the coking and the argumentation is the same as before for iron oxide.

### Gas conversion in ceria oxidation

As mentioned above suitable  $\text{H}_2\text{O}$  and  $\text{CO}_2$  conversions in the oxidation of Ceria were determined by parameter variation. For that purpose we repeat the simulation in the region of the highest efficiency found in Figs. 8 and 9 for different conversions. For SMR conversions of  $X_{\text{H}_2\text{O}} = 0.5, 0.7, 0.9, 0.99$  and for DMR conversions of  $X_{\text{CO}_2} = 0.9, 0.95, 0.99$  are studied. For DMR we only study high conversions, since we expect the disadvantages of a low conversion to be higher than for SMR. The reasons for this assumption are: First of all remaining  $\text{CO}_2$  in the product stream is more challenging to separate than remaining  $\text{H}_2\text{O}$ , which means the conversion has a higher importance in terms of product purity in case of DMR. Also a low  $X_{\text{CO}_2}$  leads to high compression work, since both feed and product have a high volume flow. This effect is less significant for SMR since pumping of the liquid water feed has a low energy demand and excess water in the product can be removed easily by a flash prior to the second compression (see Fig. 2).

In addition to varying the conversion, we exploit the temperature to the highest value at which the model still converges in order to find the efficiency maximum with respect to the oxidation temperature. The limit on  $T_{ox}$  is not constant, but depends on the value of  $T_{red}$  (higher  $T_{red}$  allow for higher  $T_{ox}$ ). This results in the cascade-shaped area of unknown values in Fig. 10 and Fig. 11 (hatched area). The figures also include a black line, which represents points, at which  $T_{red} = T_{ox}$ , i.e. isothermal operation of the process.

In Fig. 10 we find that the efficiency rises with rising  $T_{ox}$  and reaches its local maximum beyond isothermal operation, i.e.  $T_{red} < T_{ox}$ . At this point the oxidation is autothermal and increasing  $T_{ox}$  means feeding a hotter ceria stream into the reduction chamber and thereby making the heat of reaction of the exothermal oxidation available in the allothermal reduction step. The efficiency is typically the highest, at the oxidation temperature that marks the transition from an autothermal to an allothermal oxidation step. Here the aforementioned benefit due to high oxidation temperatures and the additional solar heat applied to the oxidation chamber offset. Additionally the very high oxidation temperatures result in high reradiation losses. Consequently a further increase of oxidation temperatures leads to a decreasing efficiency.



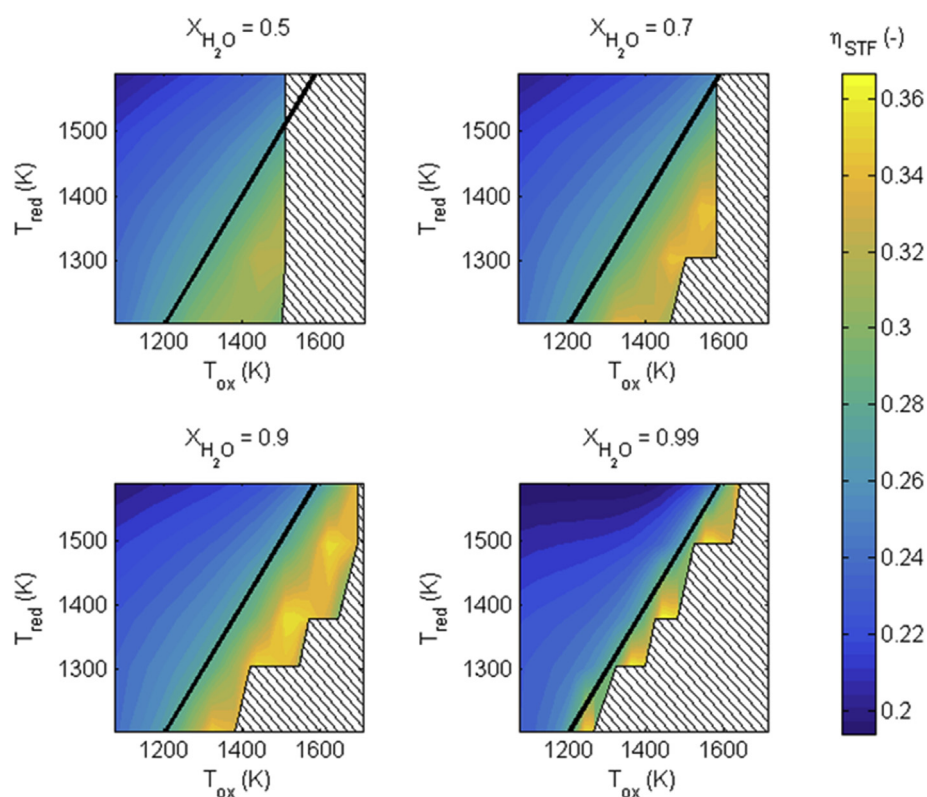


Fig. 10 – Solar-to-fuel efficiency of redox SMR with ceria as a function of reduction and oxidation temperature for different  $H_2O$ -conversions. Black line:  $T_{red} = T_{ox}$ .

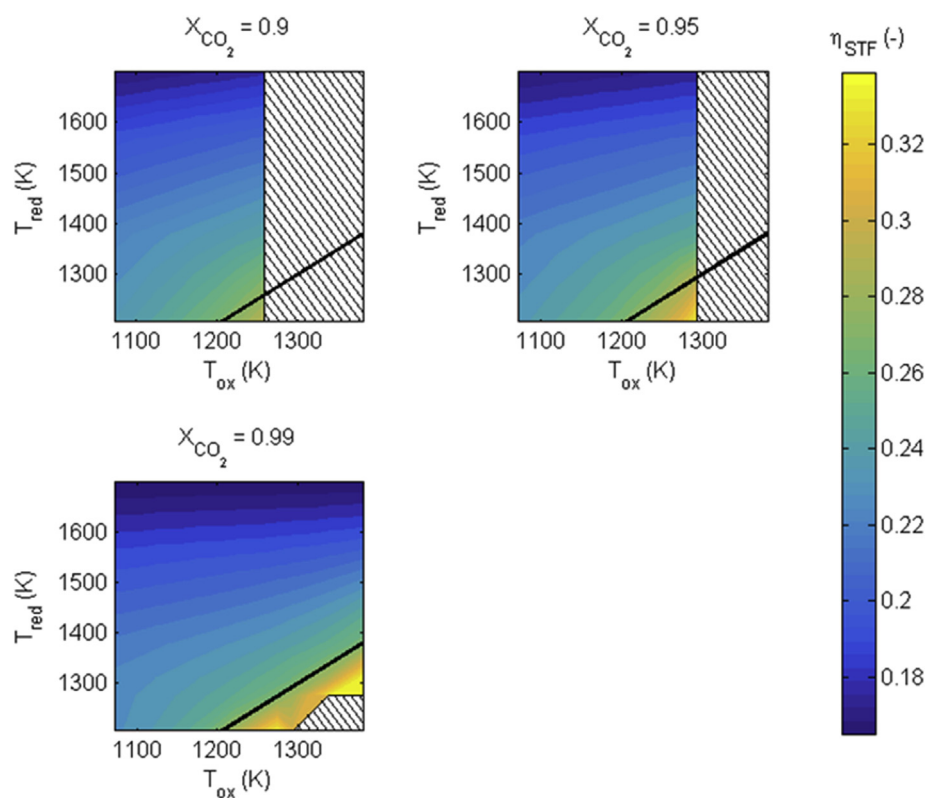


Fig. 11 – Solar-to-fuel efficiency of redox DMR with ceria as a function of reduction and oxidation temperature for different  $CO_2$ -conversions. Black line:  $T_{red} = T_{ox}$ .

Furthermore Fig. 10 shows a line of maximum efficiencies that is almost parallel to the black line that marks isothermal operation. On this line the efficiency only varies slightly. In other words: as long as the temperature difference is constant, temperatures can be changed without significantly changing the efficiency. This indicates, that the predominant effect on the efficiency is heating ceria from  $T_{ox}$  to  $T_{red}$ . In addition the slope perpendicular to the isothermal line increases at high conversions. This is because at a higher conversion, a lower oxygen partial pressure is reached in the oxidation chamber (cf. [46]). According to the correlation between oxygen partial pressure and non-stoichiometry [2] this leads to lower  $\Delta\delta$  and consequently to an increasing mass flow of ceria. On the one hand this increases the heat demand at  $T_{ox} < T_{red}$ , decreasing the efficiency. On the other hand at  $T_{ox} > T_{red}$  more sensible heat is stored in the ceria and fed to the reduction, which enhances the increase in efficiency with rising oxidation temperatures according to the explanation above. Furthermore Fig. 10 shows that the peak efficiencies move closer to the isothermal mode with increasing  $X_{H_2O}$ . At high conversions the high amount of ceria requires much heat, while due to the proportionally lower  $\Delta\delta$  the available heat of reaction stays more or less the same. Hence the oxidation becomes allothermal already at lower oxidation temperatures and from that point on the efficiency drops quickly.

The highest efficiency for each conversion is summarized in Table 1. From the table it becomes clear that a high conversion is advantageous, but the difference between  $X_{H_2O} = 0.90$  and  $0.99$  is small. In SMR the overall highest efficiency is 36.7% found at the highest conversion  $X_{H_2O} = 0.99$ .

The efficiency of DMR depicted in Fig. 11 shows a behavior similar to SMR and the discussion given above seems to apply for Fig. 11 as well. The plot however reveals large areas of unknown values for DMR.

Table 1 shows no significant difference between  $X_{CO_2} = 0.95$  and  $0.99$ , in terms of efficiency, but in comparison to  $X_{CO_2} = 0.9$ , a high conversion seems to be beneficial. On the other hand higher  $X_{CO_2}$  increase the chance of coking. However again at the most efficient points of operation no coking was found. The overall highest efficiency for DMR is 33.9% at  $X_{CO_2} = 0.99$ .

Even though the increased conversion results in higher solar-to-fuel efficiencies, the efficiencies of the reference models are not reached by the ceria-based redox cycles. Furthermore up to this point the processes were discussed in terms of efficiency. Large solid streams that are necessary, due to low  $\Delta\delta$  at high  $X_{H_2O/CO_2}$  might also have a negative impact on plant dimensioning and investment costs. Also

even though a higher conversion results in less excess reagents, it might result in larger plant dimensions and investment costs due to longer residence times. This however depends on the actual reactor design and the so far poorly understood kinetics. The latter might especially impact the results at very high  $T_{ox}$  or very low  $T_{red}$ .

### Solid-solid heat recuperation

For two-step solar-thermochemical cycles that utilize a thermal reduction step, the need for solid-solid heat recovery has been expressed in several studies [12,26,47,48]. For these processes the temperature gap between reduction and oxidation is large, so that the sensible heat consumed by the redox material is a significant portion of the process' overall energy demand. However, as mentioned above, the temperature gap in redox reforming is significantly lower and in some cases the oxidation temperature might even exceed the reduction temperature. This raises the question whether a solid-solid heat exchanger according to Fig. 2 can still improve the system efficiency in redox reforming. A parameter variation of the heat recovery rate  $\epsilon$  is performed. Herein  $\epsilon$  is defined as the ratio of actually transferred heat to the possible maximum of transferred heat. The heat exchanger's design is not studied. For possible heat exchanger designs the reader is referred to the relevant literature [48–54].

Results for SMR with iron oxide are given in Fig. 12. The application of a heat exchanger only shows a significant impact at high reduction and low oxidation temperatures as can be seen in Fig. 12 (a). Under these conditions two effects occur: Firstly, the temperature gap is the highest and with it the potential for heat recovery. Secondly, the oxidation works autothermal. At most points of operation, however, the oxidation works allothermal, i.e. it has to be irradiated. In those cases the heat exchanger simply shifts the energy demand from the reduction to the oxidation instead of saving heat. The heat exchanger still has a minor benefit in that case, since the oxidation is heated at lower temperatures than the reduction, which reduces reradiation losses. This slight difference is depicted in Fig. 12 (b). For the aforementioned autothermal state however, heat can be recuperated instead of removing it from the system by cooling the oxidation reactor. Solid-solid heat recovery increases the maximum solar-to-fuel efficiency from 41.9% without heat exchanger to 43.6% at  $\epsilon = 1$ . With respect to the literature [48,51,55] a more realistic value for  $\epsilon$  would be below 0.75. In that case the efficiency with heat exchange would be at best 43.1% according to our model. Hence, we find a relatively low impact of the heat exchanger of approximately 1 %-pt efficiency increase.

Due to the endothermal oxidation reaction in DMR with iron oxide, reduction and oxidation are both allothermal at all points of operation that were studied. As explained above for SMR this means that the heat demand is rather shifted from one reactor to the other than saved, when applying a heat exchanger. Therefore the impact of heat recovery is small for DMR with iron oxide, as shown in Fig. 13 (a) and (b). Only at very high oxidation temperatures given in Fig. 13 (a) heat recovery improves the efficiency noticeably. This seems to be due to reduced reradiation, which becomes more significant with high temperatures. In the region of the peak efficiency,

**Table 1 – Highest solar-to-fuel efficiency of ceria-based cycles and their according temperatures for different conversions.**

Process	$X_{H_2O/CO_2}$	Highest $\eta_{STF}$ (%)	$T_{red}(K)$	$T_{ox}(K)$
SMR	0.50	32.5	1305	1443
SMR	0.70	34.9	1380	1543
SMR	0.90	36.1	1380	1533
SMR	0.99	36.7	1380	1441
DMR	0.90	29.4	1204	1258
DMR	0.95	33.5	1204	1293
DMR	0.99	33.9	1310	1381

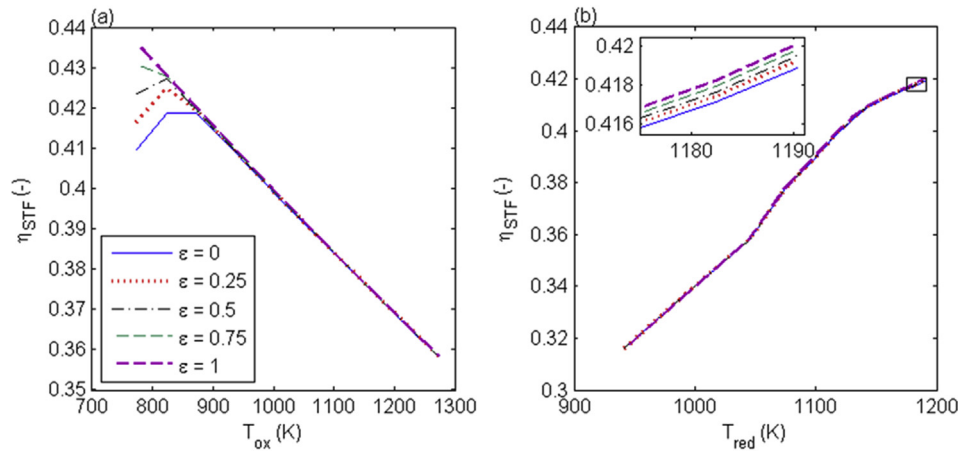


**Fig. 12 – Solar-to-fuel efficiency of redox SMR with iron oxide as a function of (a) oxidation and (b) reduction temperature. (a) Constant  $T_{red}$ . (b) Constant  $T_{ox}$ . The constant temperature is set to the best value according to Table 2.**

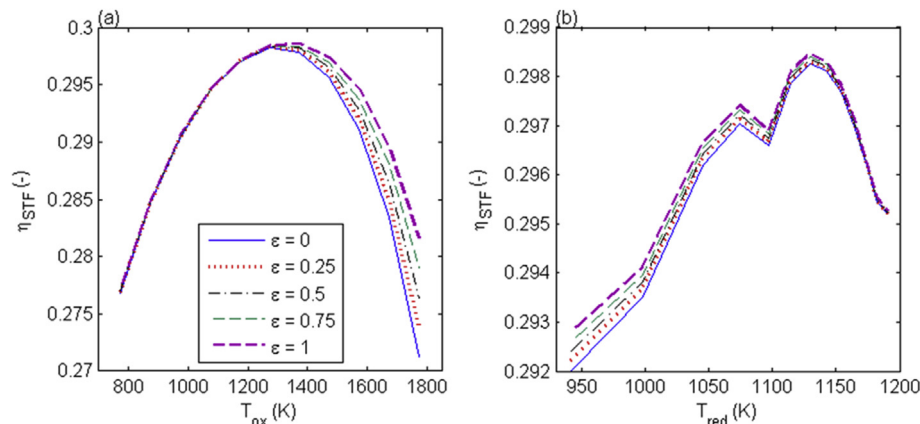
however the impact of the heat exchanger is negligible: The magnitude of the maximum solar-to-fuel efficiency is not influenced, it only moves to a higher oxidation temperature of 1373 K instead of 1273 K. Hence, solid-solid heat recuperation doesn't seem promising for redox DMR with iron oxide.

The SMR and DMR redox cycles with ceria are similar to each other. Using a heat exchanger decreases the dependence on  $T_{red}$  and  $T_{ox}$  and flattens the curves shown in Fig. 14 and Fig. 15. Heat exchange improves the performance for all points of operation with  $T_{ox} < T_{red}$ . Here heat is recuperated as explained for SMR with iron oxide. For  $T_{ox} = T_{red}$  the performance of a system with and one without heat exchanger is identical, because no heat can be exchanged between the two material streams. Operation without heat exchanger is advantageous if  $T_{ox} > T_{red}$ . Here, the heat exchanger preheats the solid, which enters the oxidation. The exothermal oxidation is typically cooled and the transferred heat is wasted. Without heat exchange the solid fed to the reduction is hotter and adds a heat source to the allothermal reduction step. In a sense, the exothermal heat of reaction of the oxidation is utilized in the reduction step, which decreases the demand of external heating. In this context the ceria cycles differ from the iron oxide cycles in that the oxidation is autothermal, usually even

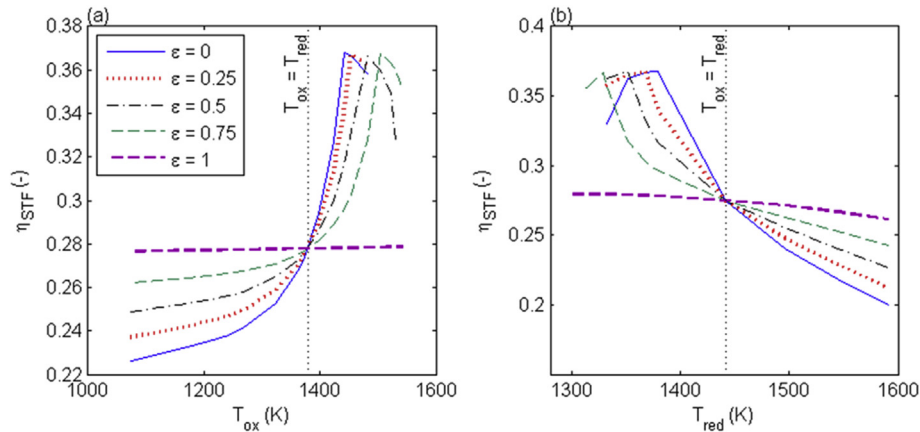
if  $T_{ox} > T_{red}$ . In summary it is only beneficial not to have a heat exchanger if the oxidation is autothermal and operated at a higher temperature than the reduction. This can only be the case for ceria cycles, but never for iron oxide cycles. Under extreme conditions, where  $T_{ox} \gg T_{red}$  also ceria cycles become allothermal and the efficiency without heat exchanger drops drastically as explained in the context of Fig. 10. In a real reactor this might already happen at lower  $T_{ox}$ , due to additional heat losses that we did not consider. Therefore, depending on the receiver and reactor design, application of a solid-solid heat exchanger might still be justified. All in all, with our model the highest efficiency for ceria cycles are achieved without a solid-solid heat exchanger. Since no significant improvements were made by the heat exchanger in any process, we do not consider solid-solid heat exchange in the following sections.

### Solar heat flux

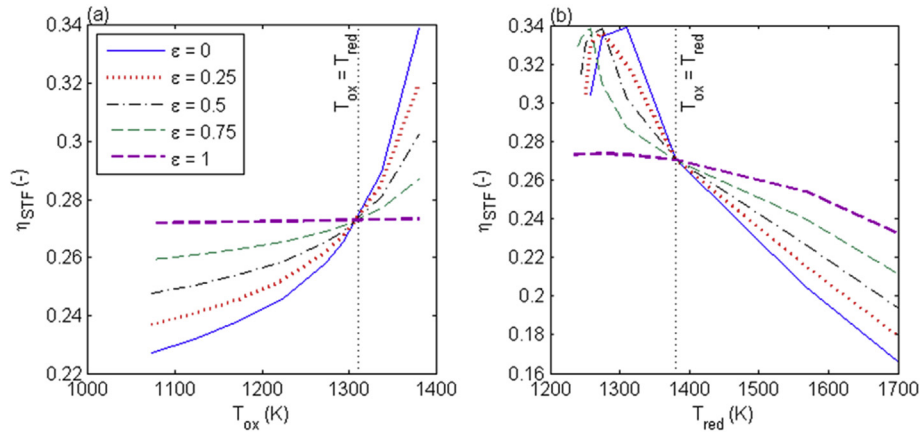
We studied heat fluxes of 1500 and 1000 kW/m<sup>2</sup> to analyze the impact on the system's efficiency. In general a high solar heat flux increases the receiver efficiency and favors high temperatures, due to an increased heat input in relation to reradiation



**Fig. 13 – Solar-to-fuel efficiency of redox DMR with iron oxide as a function of (a) oxidation and (b) reduction temperature. (a) Constant  $T_{red}$ . (b) Constant  $T_{ox}$ . The constant temperature is set to the best value according to Table 2.**



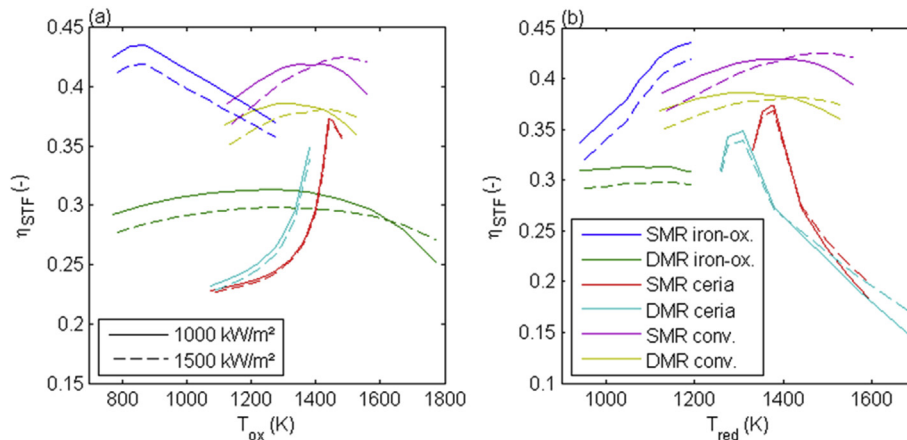
**Fig. 14** – Solar-to-fuel efficiency of redox SMR with ceria as a function of (a) oxidation and (b) reduction temperature. (a) Constant  $T_{red}$ . (b) Constant  $T_{ox}$ . The constant temperature is set to the best value according to Table 2.



**Fig. 15** – Solar-to-fuel efficiency of redox DMR with ceria as a function of (a) oxidation and (b) reduction temperature. (a) Constant  $T_{red}$ . (b) Constant  $T_{ox}$ . The constant temperature is set to the best value according to Table 2.

losses. On the other hand it is accompanied by decreased annual field efficiencies. The latter were calculated in HFLCAL to be 60.22% for 1500 kW/m<sup>2</sup> and 64.88% for 1000 kW/m<sup>2</sup>. Fig. 16(a) and (b) show the solar-to-fuel efficiency for both heat fluxes.

Conventional processes are included for reference. The temperature in that case is the reformer temperature. In fact we see the trade-off between field and receiver efficiency. Accordingly a high flux is advantageous at higher temperatures. However,

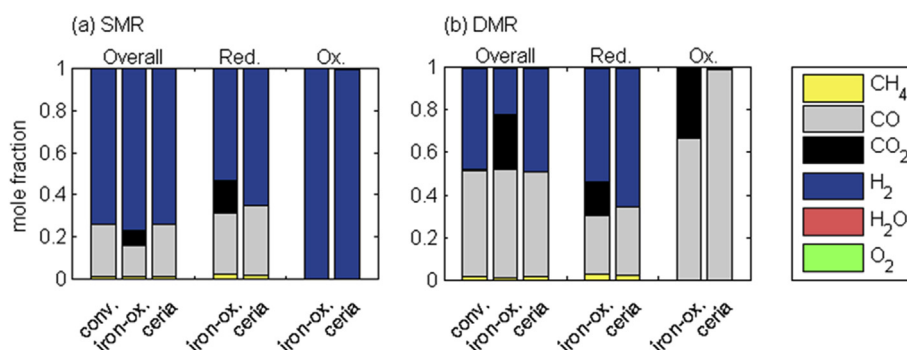


**Fig. 16** – Solar to fuel efficiency as a function of the (a) oxidation and (b) reduction temperature. In case of the conventional process the temperature is the reformer temperature in both graphs. For redox reforming: (a) constant  $T_{red}$ . (b) Constant  $T_{ox}$ . The constant temperature is set to the best value according to Table 2.



**Table 2 – Highest solar-to-fuel efficiencies found and according parameters.**

Process	Specification	Highest $\eta_{STF}$ (%)	Pressure (MPa)	Temperature (K)	
Conventional SMR	$\dot{Q}_{solar} = 1500 \text{ kW/m}^2$	42.5	2	1488	
Conventional DMR	$\dot{Q}_{solar} = 1000 \text{ kW/m}^2$	38.6	0.76	1328	
SMR with iron oxide	$\dot{Q}_{solar} = 1000 \text{ kW/m}^2$	43.5	3	1190 (red.)	873 (ox.)
DMR with iron oxide	$\dot{Q}_{solar} = 1000 \text{ kW/m}^2$	31.3	1.5	1130 (red.)	1273 (ox.)
SMR with ceria	$X_{H_2O} = 0.99$	37.3	0.25	1380 (red.)	1441 (ox.)
DMR with ceria	$\dot{Q}_{solar} = 1000 \text{ kW/m}^2$	34.9	0.18	1310 (red.) 1381 (ox.)	
	$X_{CO_2} = 0.99$				
	$\dot{Q}_{solar} = 1000 \text{ kW/m}^2$				

**Fig. 17 – Product composition at the most efficient point of operation found for each process. (a) SMR processes, (b) DMR processes.**

except conventional SMR, all processes show the highest efficiency at the lower solar flux. Fig. 16 also reveals that SMR with iron oxide is the only redox cycle that reaches a higher solar-to-fuel efficiency than the respective conventional process. On top of that it can be performed at lower temperatures. DMR with iron oxide on the other hand yields the lowest peak efficiency of all processes. This can be explained by a lower gain in HHV, than in the other processes, due to product impurities, which are discussed in the next section. Furthermore, in terms of efficiency both ceria cycles are outperformed by the conventional processes. The highest efficiencies are summarized in Table 2.

### Product quality

To complete our comparison of the different processes we also consider the product quality. One aspect of the product quality is the methane concentration in the product. It is kept at about 1.5% or less by setting the methane conversion to 94.2%. Different product-selectivities of iron oxide and ceria can however still result in different product compositions.

In redox reforming, the reduction and oxidation chambers have separated product streams that can be utilized individually. For comparison with the conventional process we introduce the overall product composition: a hypothetical mixture of both product streams, independent on whether they are actually mixed or not. Fig. 17 shows the overall product composition, the composition of the reduction product and the composition of the oxidation product for all processes.

While the overall product of ceria cycles has a similar composition to conventional reforming, the iron oxide cycles yield less CO and show a significant content of CO<sub>2</sub>. One reason is the conversion of CH<sub>4</sub> to CO<sub>2</sub> during the reduction, which is represented by the CO<sub>2</sub> content in the reduction

product. For DMR a second reason is unconverted CO<sub>2</sub> in the oxidation. For iron oxide there is a thermodynamic limitation to less than 68% of CO<sub>2</sub> being converted to CO. This we calculated with values of  $\Delta G_R^0(T)$  of reaction (1.2) for temperatures up to 2500 K in FactSage. Consequently we find a notable CO<sub>2</sub> content of the oxidation product given in Fig. 17 (b). The graph shows further that in case of ceria CO<sub>2</sub> is almost fully converted as discussed above. This is an advantage that ceria has over iron oxide. Fig. 17 (a) shows that the oxidation product of both redox SMR alternatives is almost pure hydrogen. After a single-stage flash separation the iron oxide cycle yields a 99.9% H<sub>2</sub> stream, while in the ceria cycle 1% of water remains in the product.

### Solid-phase composition of iron oxide

After the simulations we checked our assumption that no FeO is formed during the reduction. Equilibria of relevant points of operation shown in Fig. 16 were calculated in FactSage. We find that the main product in the solid phase is metallic Fe as assumed. However, also FeO is formed. High reduction temperatures, low pressures and high CH<sub>4</sub>/Fe ratios promote the reduction to Fe. For the aforementioned points of operation the reduced solid phase consists of 86–95% Fe and 5–14% FeO. We attribute the production of FeO mainly to lower CH<sub>4</sub>/Fe ratios than originally expected.

### Conclusion

Process simulations of iron oxide and ceria-based solar driven redox cycles for SMR and DMR as well as reference processes

are performed in ACM. From the results we draw the following conclusions:

1. Redox SMR with iron oxide is the only redox cycle of the investigated cases that shows a higher solar-to-fuel efficiency than the reference process. Also it can be performed at lower temperatures. All other redox cycles are outperformed by the conventional approaches.
2. A solid-solid heat exchanger has only minor impact on the peak solar-to-fuel efficiency of iron oxide-based cycles. For ceria-based cycles it might even be counterproductive. This is the case since we find the highest efficiency for ceria cycles at points of operation, where  $T_{ox} > T_{red}$ . Here, the heat exchanger decreases the efficiency. If the process is performed with  $T_{ox} < T_{red}$ , for example due to kinetics, or if unconsidered heat losses make the oxidation allothermal, the heat exchanger can improve the efficiency. Our results reveal the difference between cycles based on thermal reduction and redox reforming. The higher degree of reduction in redox reforming allows a lower oxidation degree and therefore higher oxidation temperatures. At the same time, the reductant allows lower reduction temperatures. These conditions lead to a different behavior of the system.
3. A solar heat flux of 1000 kW/m<sup>2</sup> from the field leads to a higher peak efficiency than 1500 kW/m<sup>2</sup> for all processes, but conventional SMR. Usually the higher field efficiency outweighs the lower receiver efficiency.
4. Compared to conventional reforming, the syngas produced in iron oxide-based cycles shows significant amounts of CO<sub>2</sub>. Ceria-based cycles yield a syngas of almost the same composition as conventional reforming. In redox reforming, two separated product streams occur. Therefore, for SMR with both iron oxide and ceria, highly pure hydrogen can be accessed without challenging separation steps. DMR with ceria might be an interesting niche application for the Production of high purity CO.

In summary we show that solar redox reforming cycles can be operated without solid-solid heat exchangers, which are yet to be fully developed. Together with some potential advantages over conventional solar reforming, this makes solar redox reforming an interesting transition technology towards solar redox cycles with a thermal reduction step. In potential future studies spatially resolved reactor models, estimation of convective heat losses and consideration of FeO formation would help to further increase the accuracy of calculated efficiencies.

## Acknowledgements

This work has received funding from the Helmholtz Association within the Virtual Institute SolarSyngas (VH-VI-509). In addition, the work was carried out with financial support from European Union through EFRE under contract EFRE-0800578 (INDIREF). The authors would like to thank Dr. Josua Vieten for many fruitful discussions.

## REFERENCES

- [1] Buelens LC, et al. Super-dry reforming of methane intensifies CO<sub>2</sub> utilization via Le Chatelier's principle. *Science* 2016;354(6311):449–52.
- [2] Bulfin B, et al. Analytical model of CeO<sub>2</sub> oxidation and reduction. *J Phys Chem C* 2013;117(46):24129–37.
- [3] Ermanoski I. Maximizing efficiency in two-step solar-thermochemical fuel production. *Energy Procedia* 2015;69:1731–40.
- [4] Lange M, et al. Efficiency assessment of a two-step thermochemical water-splitting process based on a dynamic process model. *Int J Hydrogen Energy* 2015;40(36):12108–19.
- [5] Venstrom LJ, et al. The effects of morphology on the oxidation of ceria by water and carbon dioxide. *J Sol Energy Eng* 2012;134(1):011005.
- [6] Ackermann S, et al. Reticulated porous ceria undergoing thermochemical reduction with high-flux irradiation. *Int J Heat Mass Transf* 2017;107:439–49.
- [7] Jeong HH, et al. Stepwise production of syngas and hydrogen through methane reforming and water splitting by using a cerium oxide redox system. *Int J Hydrogen Energy* 2011;36(23):15221–30.
- [8] Go KS, Son SR, Kim SD. Reaction kinetics of reduction and oxidation of metal oxides for hydrogen production. *Int J Hydrogen Energy* 2008;33(21):5986–95.
- [9] Kodama T, Gokon N. Thermochemical cycles for high-temperature solar hydrogen production. *Chem Rev* 2007;107(10):4048–77.
- [10] Chueh WC, et al. High-flux solar-driven thermochemical dissociation of CO<sub>2</sub> and H<sub>2</sub>O using nonstoichiometric ceria. *Science* 2010;330:1797–801.
- [11] Abanades S, et al. Investigation of reactive cerium-based oxides for H<sub>2</sub> production by thermochemical two-step water-splitting. *J Mater Sci* 2010;45(15):4163–73.
- [12] Marxer D, et al. Solar thermochemical splitting of CO<sub>2</sub> into separate streams of CO and O<sub>2</sub> with high selectivity, stability, conversion, and efficiency. *Energy Environ Sci* 2017;10:1142–9.
- [13] Bulfin B, et al. Thermodynamics of CeO<sub>2</sub> thermochemical fuel production. *Energy Fuels* 2015;29(2):1001–9.
- [14] Bulfin B, et al. Solar thermochemical hydrogen production using ceria zirconia solid solutions: efficiency analysis. *Int J Hydrogen Energy* 2016;41(42):19320–8.
- [15] Bulfin B, et al. Applications and limitations of two step metal oxide thermochemical redox cycles; a review. *J Mater Chem* 2017;5(36):18951–66.
- [16] Grobber J, et al. Heat transfer in a directly irradiated ceria particle bed under vacuum conditions. *Sol Energy* 2017;158:737–45.
- [17] Brendelberger S, et al. Counter flow sweep gas demand for the ceria redox cycle. *Sol Energy* 2015;122:1011–22.
- [18] Zhu L, Lu Y, Shen S. Solar fuel production at high temperatures using ceria as a dense membrane. *Energy* 2016;104:53–63.
- [19] Meredig B, Wolverton C. First-principles thermodynamic framework for the evaluation of thermochemical H<sub>2</sub> O<sub>2</sub>-or CO<sub>2</sub>-splitting materials. *Phys Rev B* 2009;80(24):245119.
- [20] Takacs M, Scheffe JR, Steinfeld A. Oxygen nonstoichiometry and thermodynamic characterization of Zr doped ceria in the 1573–1773 K temperature range. *Phys Chem Chem Phys* 2015;17(12):7813–22.
- [21] Krenzke PT, Fosheim JR, Davidson JH. Solar fuels via chemical-looping reforming. *Sol Energy* 2017;156:48–72.

- [22] He F, et al. A hybrid solar-redox scheme for liquid fuel and hydrogen coproduction. *Energy Environ Sci* 2014;7(6):2033–42.
- [23] Vieten J, et al. Redox behavior of solid solutions in the  $\text{SrFe}_{1-x}\text{Cu}_x\text{O}_{3-\delta}$  system for application in thermochemical oxygen storage and air separation. *Energy Technology*; 2018.
- [24] Carrillo RJ, Scheffe JR. Advances and trends in redox materials for solar thermochemical fuel production. *Sol Energy* 2017;156:3–20.
- [25] Panlener RJ, Blumenthal RN, Garnier JE. A thermodynamic study of nonstoichiometric cerium dioxide. *J Phys Chem Solids* 1975;36(11):1213–22.
- [26] Muhich CL, et al. Comparing the solar-to-fuel energy conversion efficiency of ceria and perovskite based thermochemical redox cycles for splitting  $\text{H}_2\text{O}$  and  $\text{CO}_2$ . *Int J Hydrogen Energy* 2018;43(41):18814–31.
- [27] Sheu EJ, Ghoniem AF. Redox reforming based, integrated solar-natural gas plants: reforming and thermodynamic cycle efficiency. *Int J Hydrogen Energy* 2014;39(27):14817–33.
- [28] Sheu EJ, Mokheimer EM, Ghoniem AF. Dry redox reforming hybrid power cycle: performance analysis and comparison to steam redox reforming. *Int J Hydrogen Energy* 2015;40(7):2939–49.
- [29] Fischer F, Tropsch H. Über die Herstellung synthetischer Ölgemische (Synthol) durch Aufbau aus Kohlenoxyd und Wasserstoff. *Brennst. Chem* 1923;4:276–85.
- [30] Warren KJ, et al. Theoretical and experimental investigation of solar methane reforming through the nonstoichiometric ceria redox cycle. *Energy Technol* 2017;5(11):2138–49.
- [31] Welte M, et al. Combined Ceria reduction and methane reforming in a solar-driven particle-transport reactor. *Ind Eng Chem Res* 2017;56(37):10300–8.
- [32] Montes M, et al. Solar multiple optimization for a solar-only thermal power plant, using oil as heat transfer fluid in the parabolic trough collectors. *Sol Energy* 2009;83(12):2165–76.
- [33] Birnbaum J, et al. A direct steam generation solar power plant with integrated thermal storage. *J Sol Energy Eng* 2010;132(3):031014.
- [34] Takenaka S, Hanaizumi N, Otsuka K. Production of pure hydrogen from methane mediated by the redox of Ni- and Cr-added iron oxides. *J Catal* 2004;228(2):405–16.
- [35] Steinfeld A, Kuhn P, Karni J. High-temperature solar thermochemistry: production of iron and synthesis gas by  $\text{Fe}_3\text{O}_4$ -reduction with methane. *Energy* 1993;18(3):239–49.
- [36] Otsuka K, et al. Production of hydrogen from methane without  $\text{CO}_2$ -emission mediated by indium oxide and iron oxide. *Int J Hydrogen Energy* 2001;26(3):191–4.
- [37] Bale CW, et al. FactSage thermochemical software and databases, 2010–2016. *Calphad* 2016;54:35–53.
- [38] Agrafiotis C, et al. Solar thermal reforming of methane feedstocks for hydrogen and syngas production—a review. *Renew Sustain Energy Rev* 2014;29:656–82.
- [39] Von Storch H, Becker-Hardt S, Sattler C. (Solar) mixed reforming of methane: potential and limits in utilizing  $\text{CO}_2$  as feedstock for syngas production—a thermodynamic analysis. *Energies* 2018;11(10):2537.
- [40] Rostrup-Nielsen JR, Sehested J, Nørskov JK. Hydrogen and synthesis gas by steam- and  $\text{CO}_2$  reforming. 2002.
- [41] Schwarzbözl P, Pitz-Paal R, Schmitz M. Visual HFLCAL-A software tool for layout and optimisation of heliostat fields. Proceedings of 15th SolarPACES Conference, Berlin, Germany (15 – 18 September 2009) 2009.
- [42] Hottel HC. A simple model for estimating the transmittance of direct solar radiation through clear atmospheres. *Sol Energy* 1976;18(2):129–134.
- [43] Press W, et al. Numerical recipes in FORTRAN77: the art of scientific computing. Cambridge University Press; 1986.
- [44] Bartholomew, C.H. and R.J. Farrauto, Fundamentals of industrial catalytic processes. 2<sup>nd</sup> ed. 2006, Hoboken, N.J.: Wiley. xxiii, 966 p.
- [45] Atkins P, Paula Jd. Physical chemistry. 9th ed 2009.
- [46] Lange M, et al. T–S diagram efficiency analysis of two-step thermochemical cycles for solar water splitting under various process conditions. *Energy* 2014;67:298–308 (0).
- [47] Lapp J, Davidson J, Lipiński W. Efficiency of two-step solar thermochemical non-stoichiometric redox cycles with heat recovery. *Energy* 2012;37(1):591–600.
- [48] Brendelberger S, et al. Performance assessment of a heat recovery system for monolithic receiver-reactors. *J Sol Energy Eng* 2019;141(2). 021008-021008-9.
- [49] Diver RB, et al. Solar thermochemical water-splitting ferrite-cycle heat engines. *J Sol Energy Eng* 2008;130(4):41001–8.
- [50] Lapp J, Davidson JH, Lipiński W. Heat transfer analysis of a solid-solid heat recuperation system for solar-driven nonstoichiometric redox cycles. *J Sol Energy Eng* 2013;135(3):031004.
- [51] Felinks J, et al. Heat recovery concept for thermochemical processes using a solid heat transfer medium. *Appl Therm Eng* 2014;73(1):1004–11.
- [52] Ermanoski I, Siegel NP, Stechel EB. A new reactor concept for efficient solar-thermochemical fuel production. *J Sol Energy Eng* 2013;135(3):031002.
- [53] Budama VK, et al. Thermodynamic development and design of a concentrating solar thermochemical water-splitting process for co-production of hydrogen and electricity. *Int J Hydrogen Energy* 2018;43(37):17574–87.
- [54] Siegrist S, et al. Moving brick receiver–reactor: a solar thermochemical reactor and process design with a solid–solid heat exchanger and on-demand production of hydrogen and/or carbon monoxide. *J Sol Energy Eng* 2019;141(2).
- [55] Falter CP, Pitz-Paal R. A generic solar-thermochemical reactor model with internal heat diffusion for counter-flow solid heat exchange. *Sol Energy* 2017;144:569–79.